Size-Dependent Tumor Penetration and *in Vivo* Efficacy of Monodisperse Drug−Silica Nanoconjugates

Li Tang,[†] Nathan P. Gabrielson,[†] Fatih M. Uckun,[§,¶] Timothy M. Fan,[‡] and Jianjun Cheng*,[†]

[†]Department of Materials Science and Engineering and [‡]Department of Veterinary Clinical Medicine, University of Illinois at Urbana−Champaign, 1304 West Green Street, Urbana, Illinois 61801, United States
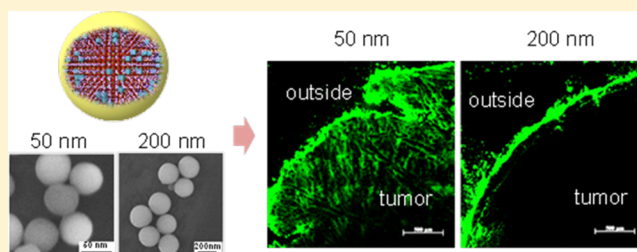
[§]Developmental Therapeutics Program, Children's Center for Cancer and Blood Diseases, Children's Hospital Los Angeles, Los Angeles, California 90027, United States

[¶]Developmental Therapeutics Program, Norris Comprehensive Cancer Center, University of Southern California Keck School of Medicine, Los Angeles, California 90027, United States

Ⓢ Supporting Information

ABSTRACT: The size of a nanomedicine strongly correlates with its biodistribution, tissue penetration, and cell uptake. However, there is limited understanding how the size of nanomedicine impacts the overall antitumor efficacy. We designed and synthesized camptothecin−silica nanoconjugates (Cpt−NCs) with monodisperse particle sizes of 50 and 200 nm, two representative sizes commonly used in drug delivery, and evaluated their antitumor efficacy in murine tumor models. Our studies revealed that the 50 nm Cpt−NC showed higher anticancer efficacy than the larger analogue, due presumably to its faster cellular internalization and more efficient tumor accumulation and penetration. Our findings suggest that nanomedicine with smaller sizes holds great promise for improved cancer therapy.

KEYWORDS: *cancer, drug delivery, nanoconjugates, silica nanoparticles, size effect*

INTRODUCTION

Therapeutic nanomedicines, drug-containing nanostructures exemplified by micelles and nanoparticles (NPs), typically have sizes ranging from a few to several hundred nanometers.[1−5] They are designed as modalities alternative to the conventional molecular therapeutics for disease treatment, in order to achieve enhanced efficacy and reduced side effects.[6−24] To improve the overall performance of therapeutic nanomedicines *in vivo*, there has been tremendous interest in fabricating nanomedicines with controlled physicochemical properties as well as understanding the correlation between the physicochemical properties of nanomedicines and their biological performance.[21,25−30] In the latter context, it was found that the shape of polymeric micelles greatly impacts the circulation time.[31] The surface charge of gold NPs was found to strongly affect the tissue penetration behavior.[32] Moreover, increasing evidence indicated that particle size plays a vital role in controlling systemic and lymphatic biodistribution, *in vivo* tumor targeting and penetration, and cellular trafficking of particulate drug delivery vehicles.[1,2,4,25,33] Although these fundamental studies give insightful information on the correlation of cell internalization and tissue distribution of nanomedicines with their physicochemical properties, there is limited understanding how the size of nanomedicine impacts the overall antitumor efficacy, which is crucial for further optimizing nanomedicines.

Extensively investigated nanomedicines, including Doxil and Abraxane, the two FDA-approved anticancer nanomedicines, are in the size range of ∼100−200 nm.[34,35] These nanomedicines showed limited accumulation and penetration in hypovascular tumors.[36,37] Some recent studies[1,3,38,39] demonstrated that reducing nanomedicine sizes below 60 nm could substantially improve the penetration and retention of nanomedicine in tumor tissues. It would be interesting to study nanomedicines with two discrete sizes, one above and the other below the threshold for tumor tissue penetration, while keeping all other parameters constant, to study how the size of nanomedicine correlates with their *in vitro* and *in vivo* performance, in particular the correlation of tumor tissue penetration of a nanomedicine with its antitumor efficacy. In this study, we report the systemic evaluation of the camptothecin−silica nanoparticle conjugates, termed Cpt−silica nanoconjugates (NCs), with size of 200 nm (expected to be non-tumor-penetrating) and 50 nm (expected to be tumor-penetrating), aiming to answer the question whether

smaller-sized, drug-containing NPs can indeed be more efficient in tumor tissue penetration and subsequently be more efficacious in treating cancer.

■ EXPERIMENTAL SECTION

Materials. All chemicals, including tetraethyl orthosilicate (TEOS, 99.999%) and camptothecin (Cpt), were purchased from Sigma-Aldrich (St. Louis, MO, USA) and used as received unless otherwise noted. mPEG5k-triethoxysilane (PEG-sil) (Figure 1) was purchased from Laysan Bio (Arab, AL, USA) and used as received. Rhodamine B isothiocyanate (RITC) and IR783-containing silanes were prepared as described in a previous paper.[39] HPLC analyses were performed on a System Gold system (Beckman Coulter, Fullerton, CA, USA) equipped with a 126P solvent module, a System Gold 128 UV detector, and an analytical C18 column (Luna C18, 250 × 4.6 mm, 5 μm, Phenomenex, Torrance, CA, USA). The sizes and mono-dispersities of silica NPs were determined on a Hitachi S4800 high resolution scanning electron microscope (SEM). The real time monitoring of the drug−silica NC sizes and mono-dispersities was done with a ZetaPlus dynamic light-scattering (DLS) detector (15 mW laser, incident beam = 676 nm, Brookhaven Instruments, Holtsville, NY, USA). The HeLa cells (ATCC, Manassas, VA, USA) used for cellular internalization studies were cultured in MEM medium containing 10% fetal bovine serum (FBS), 100 units/mL aqueous penicillin G, and 100 μg/mL streptomycin (Invitrogen, Carlsbad, CA, USA). LNCaP cells (ATCC) used for MTT assays were cultured in RPMI-1640 medium containing 10% FBS, 100 units/mL aqueous penicillin G, and 100 μg/mL streptomycin. The absorbance wavelength on a microplate reader (Perkin-Elmer, Victor[3] V, Waltham, MA, USA) was set at 570 nm for MTT assay. Confocal microscopy images for cell internalization studies were taken by Leica SP2 laser scanning confocal microscope (TCS SP2 RBB, Leica Microsystems, Bannockburn, IL, USA) using a 63× oil lens and an excitation wavelength of 543 nm. Prior to use in tumor inoculation, EL4 or Lewis lung carcinoma (LLC) cells were cultured in DMEM medium containing 10% FBS, 100 units/mL aqueous penicillin G, and 100 μg/mL streptomycin. For the *ex vivo* tumor penetration study, the flash frozen tumor tissue embedded with optimum cutting temperature (OCT) compound (Sakura Finetek, USA) was sectioned with a Leica CM3050S cryostat and mounted on glass slides. The tissue sections were observed on a fluorescence microscope (Zeiss Axiovert 200M, Thornwood, NY, USA). For biodistribution studies, the organs were fixed in 10% formalin and the fluorescence of the whole organ was measured using an Odyssey infrared mouse imaging system (LI-COR, Lincoln, NE, USA).

Preparation of Cpt−Silica Nanoconjugates (Cpt−NC) with Controlled Sizes.[39] Silica NPs of controlled sizes were first prepared using Stöber method.[40,41] For the preparation of 200 nm NPs, 1 mL of methanol, 0.27 mL of DI water, and 0.24 mL of concentrated ammonia were mixed. Then 62.5 μL of TEOS was added to the mixture, which was stirred gently for 24 h. The NPs were collected by centrifugation at 15k rpm and washed with ethanol (1 mL × 3). Synthetic procedures were similar for silica NPs of 50 nm, except for the amount of reagents used (i.e., 1 mL of methanol, 0.36 mL of DI water, 0.08 mL of concentrated ammonia, and 62.5 μL of TEOS). Cpt-S-sil was synthesized as previously reported.[39] To prepare Cpt-NCs of 50 and 200 nm (Cpt50 or Cpt200), silica NPs (4.1 mg), prepared with desired sizes as described above, were

redispersed in a mixture of MeOH (0.7 mL) and DI water (0.2 mL) followed by the addition of Cpt-S-sil (1.7 mg) in DMSO (100 μL). After the mixture was stirred for 10 min and homogenized, a NaF aqueous solution (25 μL, 10 mg/mL) was added. The pH of this mixture was around 7. The supernatant of the mixture was monitored by HPLC to quantify the unreacted Cpt in order to determine the incorporation efficiency of Cpt to NCs. Drug loadings were calculated based on the feeding ratio of drugs and incorporation efficiency. After reaction, without isolating the Cpt−NCs, surface modification was carried out by directly adding a methanol solution of mPEG$_{5k}$-sil (10 mg/mL) at the weight ratio of PEG$_{5k}$-sil/NC = 5/27.5. The mixture was stirred for another 12 h at rt. Surface modified NCs were collected by centrifugation at 15k rpm, and the supernatant was removed. The isolated NCs were washed with ethanol (1 mL × 3) and redispersed in DI water or phosphate-buffered saline solution (PBS, 1×) before use. The NC size and shape were characterized by SEM (Hitachi S4800, at 5 kV) and DLS.

Release Kinetics of Cpt−NCs. The NCs (Cpt50 or Cpt200) were dispersed in PBS (1×) (0.6 mg/mL), equally distributed to multiple vials with 1 mL of NC solution per vial, and then incubated at 37 °C. At selected time intervals, three vials of each group were taken out of the incubator. The NC solution was mixed with equal volume of methanol (1 mL) and centrifuged at 15k rpm for 10 min. The supernatant (1 mL) was transferred to an eppendorf tube without disturbing the precipitate (NCs) and tuned to pH 2 with phosphoric acid (85%, 100 μL). The resulting solution was directly injected into a HPLC equipped with an analytical C18 column. A mixture of acetonitrile and water (containing 0.1% TFA) at a volume ratio of 1:3 was used as the mobile phase. The flow rate was set at 1 mL/min. The area of the HPLC peak of the released Cpt (λ_{abs} = 370 nm) was integrated for the quantification of Cpt as compared to a standard curve of free Cpt. A similar release kinetics study was also performed in PBS (1×) containing 17 U/mL esterase (Sigma-Aldrich, E3019, esterase from porcine liver).

Cytotoxicity of Cpt−NCs by MTT Assay. LnCaP cells were seeded in 96-well plates at 3,000 cells/well and grown in culture medium containing 10% FBS at 37 °C for 24 h in a humidified 5% CO_2 atmosphere. The medium was replaced with fresh medium containing Cpt, Cpt−silica NCs, or blank silica NCs in concentrations ranging from 1 nM to 10 μM Cpt or equivalent (equiv.) Cpt. At each concentration, six wells per plate were treated. The cell viability was determined by MTT assay after 72 h. The standard MTT assay protocols were followed thereafter.[42]

Cellular Internalization of Silica NCs with Different Sizes. In the qualitative analysis by confocal laser scanning microscopy, HeLa cells (5 × 10^{4}) were seeded in a 4-well chamber slide for 24 h. Cells were washed once with opti-MEM and then incubated for 1 h (37 °C) with opti-MEM (1 mL) containing 100 μg/mL RITC-labeled NCs of 50 or 200 nm. The cells were then washed by PBS (1×) (1 mL) three times. Cells were then fixed with 4% paraformaldehyde and subsequently imaged by confocal laser scanning microscopy. The nucleus was stained with 4′,6-diamidino-2-phenylindole (DAPI).

In the quantitative analysis by microplate reader, HeLa cells were seeded in 24-well plates at a density of 5 × 10^{4} cells/well and cultured for 24 h. After that, the culture medium was replaced with opti-MEM and preincubated at 37 °C for 30 min
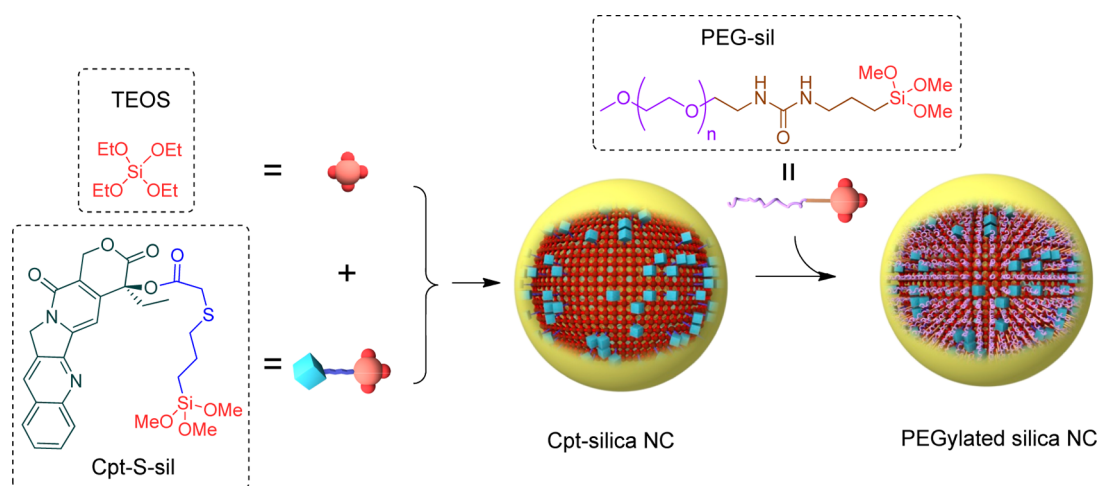
Figure 1. Schematic illustration of the preparation of size controlled PEGylated Cpt−NCs.

followed by addition of RITC-labeled NCs of 50 or 200 nm at 100 μg/mL. After incubation at 37 °C for 2 h, the medium was discarded, and cells were rinsed with PBS (1×) three times. The cells were then lysed with 0.5% SDS (pH 8.0, 500 μL/ well) at rt for 20 min. The content of RITC-labeled NCs in the lysate was quantified by microplate reader ($\lambda_{ex} = 570$ nm, $\lambda_{em} = 590$ nm). The protein content was measured using the Pierce BCA protein assay (Rockford, IL, USA). A standard curve was obtained using a bovine serum albumin (BSA) solution. The uptake level was expressed as percentage of the total fluorescence present in the feeding solution normalized by mg of protein (Figure 3b).

To explore the mechanism involved in the uptake process, cells were incubated with either the metabolic inhibitor sodium azide (0.1%) and 2-deoxyglucose (50 mM), the clathrin inhibitor chlorpromazine (10 μg/mL), the caveolar inhibitor genistein (0.2 mM) or methyl-β-cyclodextrin (m-βCD) (5.0 mM), or macropinocytosis inhibitor wortmannin (10 μg/mL) for 30 min prior to the addition of RITC-labeled NCs. Results were expressed as the percentage of the total fluorescence present in treated cells relative to untreated cells according to the quantitative procedure described above.

Animals and Tumor Models. C57BL/6 mice (female) and BALB/c nude mice (male) were purchased from Charles River (Wilmington, MA, USA). Feed and water were available *ad libitum*. The study protocol was reviewed and approved by The Illinois Institutional Animal Care and Use Committee (IACUC) of University of Illinois at Urbana−Champaign.

***In Vivo* Biodistribution Study.** BALB/c nude mice (8-week old) were injected subcutaneously on the right flank with 4×10^{6} LNCaP cells suspended in a 1:1 mixture of Hanks buffer solution (HBS) buffer and matrigel. When the tumor grew to ∼12 mm in diameter, mice bearing LnCaP tumors were divided into two groups with minimal tumor size variations between these two groups. Mice were injected intravenously (iv) with IR783-labeled NCs of 50 or 200 nm at a dose of 150 mg/kg. Mice were euthanized 24 h postinjection and fixed in 10% formalin. Whole body images were taken with the Odyssey infrared imaging system ($\lambda_{em} = 800$ nm). Mouse organs, including the tumor, liver, spleen, kidneys, heart, and lung, were harvested. The fluorescence intensity of each tissue was assayed with the Odyssey infrared imaging system directly. The measurements of the various organs were validated using a phantom of free IR783 solution on top of tissues of various

thicknesses. The thickness of all organs used for fluorescence measurement was less than 2 mm to ensure minimum 80% transmission.[39] To determine 100% dose, a dilute solution of IR783-labeled NCs was measured along with tissues at the same instrument settings. The data is presented as percent injected dose per gram of tissue (average ± standard deviation).

***In Vivo* Tumor Penetration Study.** IR783-labeled NCs of 50 or 200 nm were iv administered to C57BL/6 mice ($n = 3$) bearing EL4 tumors (size: ∼6.0−8.0 mm) at a dose of 150 mg/kg. Mice were euthanized 24 h postinjection, and their tumors were collected. Tumor sections with 2 mm thickness were collected and placed on glass slides. Fluorescent images were taken with Odyssey infrared imaging system ($\lambda_{em} = 800$ nm). The histograms of the fluorescent intensity of selected areas (indicated by the lines) in the fluorescence images of tumor sections (Figure 5a) were analyzed by Image J (Figure 5b).

***Ex Vivo* Tumor Penetration Study.** C57BL/6 mice (female, 12−13 week old) were injected subcutaneously on the right flank with 10×10^{6} EL4 cells suspended in a 1:1 mixture of HBS buffer and matrigel (BD Biosciences, Franklin Lakes, NJ, USA). When the EL4 tumor size reached ∼6.0−8.0 mm, the mice were sacrificed and their tumor tissues were harvested. Tumors were cultured *ex vivo* in cell media with IR783-labeled NCs of 50 or 200 nm for 48 h. Tumors without any treatment served as control. Tumor sections (20 μm thick) were collected by cryostat and then mounted on glass slides. Fluorescence images were taken by fluorescence microscopy ($\lambda_{ex} = 780$ nm). A tiling image was taken with fixed exposure time to show part of the edge and inside area of tumor sections. The fluorescence profile from the tumor surface to the inside was analyzed by Image J.

***In Vivo* Tumor Reduction Study.** Female C57BL/6 mice, 8-week old, were anesthetized, shaved, and injected in the right flank with 1×10^{6} LLC cells suspended in a mixture of HBS buffer and matrigel (1:1, v/v). When tumors had reached ∼300 mm^3, mice were divided into three groups ($n = 5$) with minimal weight and tumor size difference between groups. Tumor-bearing mice were treated by iv injection of PBS (1×), Cpt50 (25 mg Cpt equiv./kg), or Cpt200 (25 mg Cpt equiv./kg). Measurements of the tumor size for each animal were performed at regular intervals using calipers without knowledge of which injection each animal had received. The tumor volume for each time point was calculated according to the formula (length) × (width)^2/2. If body weight loss was beyond 20% of
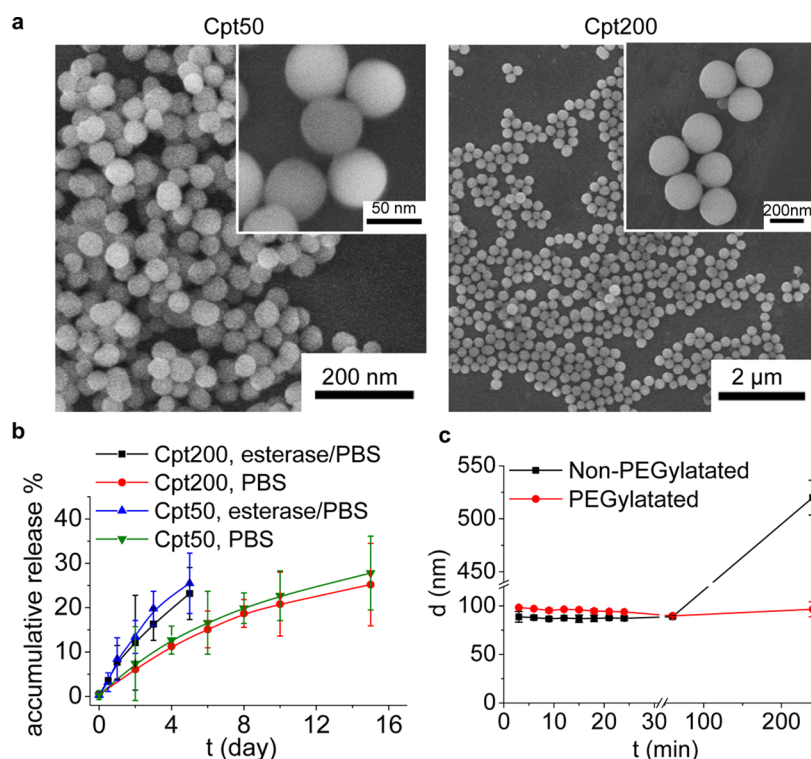
Figure 2. Characterization of Cpt−NCs. (a) SEM images of size precisely controlled Cpt−NCs. (b) Release kinetics of Cpt−NCs of two different sizes (50 and 200 nm) were compared in both PBS (1×) and PBS (1×) with 17 U/mL esterase at 37 °C. (c) Stability of PEGylated and non-PEGylated NCs in PBS (1×).

Table 1. Characterization of Cpt−NCs

	SEM[a]		DLS[b]				
name of NC	$D \pm$ SD (nm)	CV%[c]	$D \pm$ SD (nm)	PDI $\pm$ SD	IE[d] (%)	LD[e] (wt %)	IC$_{50}$[f] (nM)
Cpt50	45.7 ± 3.9	8.53	72.6 ± 0.6	0.050 ± 0.019	81.3	14.8	510
Cpt200	220.5 ± 15.5	7.03	254.0 ± 4.2	0.041 ± 0.014	80.4	14.8	800

[a]The hard core sizes were measured by SEM. D: average diameter. SD: standard deviation. [b]The hydrodynamic sizes and polydispersity (PDI) were measured by dynamic light scattering (DLS). [c]CV% = SD/D. [d]The incorporation efficiency (IE) was determined by monitoring and quantifying the concentration of free Cpt in the supernatant using HPLC by centrifuging down the NCs. [e]Real drug loading (LD) was calculated based on the feeding ratio of Cpt to NC and IE value. [f]IC$_{50}$'s of Cpt50 and Cpt200 against LnCaP cells determined by MTT assay.

the predosing weight, the animals were euthanized. When the tumor load reached 2000 mm³ or the animal had become moribund, the mouse was sacrificed. Data reported are average ± standard error of the mean.

Statistical Analyses. Student t test (two-tailed) comparisons at 95% confidence interval were used for statistical analysis. The results were deemed significant at $0.01 < *p \leq 0.05$, and highly significant at $0.001 < **p \leq 0.01$.

■ RESULTS AND DISCUSSION

Formulation and Characterization of Precisely Size-Controlled Cpt−NCs. The preparation of Cpt−NCs with precise size control is illustrated in Figure 1. We first prepared the size controlled silica NPs via controlling the concentration of TEOS, alcohol, water, and ammonia in a Stöber reaction.[39] Then, drug was incorporated using a silane-modified drug analogue under mild reaction conditions to obtain drug−NCs. In the case of the anticancer drug Cpt, the silanized derivative (Cpt-S-sil) is prepared by conjugating a trialkoxysilane group to the 20-OH group of Cpt, thereby forming an ester bond which can be hydrolyzed under physiological conditions. Finally, the

drug−NC surface can be modified using a polyethylene glycol (PEG)-containing silane compound (PEG-sil, Figure 1).

Following the protocol above, Cpt−NCs with diameters of 50 and 200 nm (denoted as Cpt50 and Cpt200 respectively, Figure 2a) were prepared. Both scanning electron microscope (SEM) and dynamic light scattering (DLS) measurements were performed to characterize the morphology, size, and size distribution of Cpt50 and Cpt200. As expected, both Cpt−NCs had excellently controlled sizes (45.7 ± 3.9 nm and 220.5 ± 15.5 nm for Cpt50 and Cpt200, respectively) and remarkably narrow size distribution with CV < 10% (CV% = SD/D) measured by SEM images (Figure 2a; Table 1). By industrial standard, particles with CV <10% are generally regarded as monodisperse.[43] The hydrodynamic diameters obtained by DLS for the two Cpt−NCs were slightly larger than the hard-core size observed by SEM. The polydispersity index (PDI) values measured by DLS also confirmed the very low dispersity of the prepared Cpt−NCs (0.050 ± 0.019 and 0.041 ± 0.014 for Cpt50 and Cpt200, respectively) (Table 1). In addition, the incorporation efficiency of Cpt was above 80% for both formulations, with drug loading as high as 14.8% being easily achieved (Table 1).
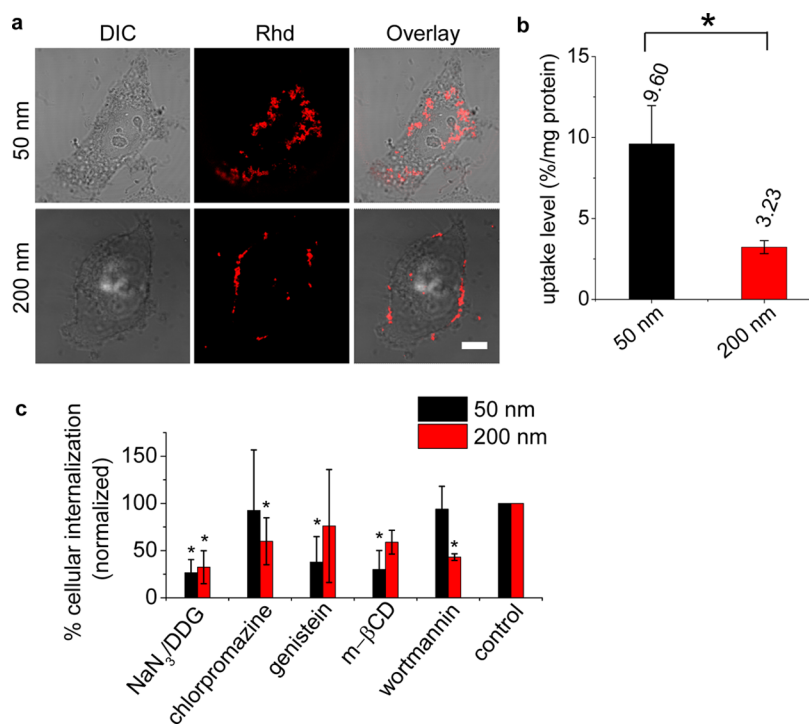
Figure 3. Cellular internalization and trafficking. (a) Confocal laser scanning microscopy images of HeLa cells after 1 h incubation at 37 °C with 50 and 200 nm silica NCs labeled with rhodamine B isothiocyanate (red). DIC: differential interference contrast. Rhd: rhodamine channel. Scale bar: 20 μm. (b) Quantitative cell uptake level of 50 and 200 nm silica NCs in HeLa cells. (%/mg of protein, average ± SD; $n = 3$; *$p < 0.05$). (c) Probing the mechanisms of cellular internalization by using inhibitors of endocytosis. Percent internalization was normalized to cell uptake level in the absence of inhibitors (average ± SD; $n = 3$; *$p < 0.05$).

Release Kinetics of Cpt from Cpt−NC. Controlled and sustained release of drug from a delivery vehicle is important for the application of nanomedicine *in vitro* and *in vivo*. The ester bond between Cpt and the silane group is degradable under physiological conditions. Thus the conjugated Cpt is expected to be released as the original form upon hydrolysis. We measured the release kinetics of Cpt−NCs in PBS (1×) as well as PBS (1×) with 17 U/mL esterase at 37 °C to mimic the physiological condition (Figure 2b). Cpt release from Cpt50 in PBS (1×) was 7.4% at day 2 and 22.7% at day 10, respectively. In the presence of esterase, which is abundant in cytoplasm, hydrolysis was accelerated and the rate of Cpt release was increased. With respect to particle size, Cpt was released slightly faster from Cpt50 as compared to Cpt200 in both PBS (1×) and PBS (1×) with 17 U/mL esterase. This is presumably due to the larger surface area of smaller NCs which exposes more drug molecules (and thus more ester linkages) to the environment as compared to larger NCs.

Stability of Cpt−NCs in PBS (1×). Particle stability against aggregation in physiological conditions is a prerequisite for effective drug delivery *in vivo*. The Cpt−NCs synthesized in this study displayed remarkable stability in PBS (1×) at 37 °C, with NC size remaining essentially unchanged for 4 h (Figure 2c). In order to increase systemic circulation half-life and reduce aggregation of NCs in blood,[44] the surface of NCs was modified by 1-(2-(2-methoxyethoxy)ethyl)-3-(3-(trimethoxysilyl)propyl)urea (PEG-sil) to introduce surface-bound PEG groups (denoted as PEGylated; Figure 1). PEGylated silica NCs were ~10 nm larger than the non-PEGylated NCs in hydrodynamic diameters (Figure 2c). When exposed to PBS (1×) for 4 h, non-PEGylated silica NCs started to aggregate and form large particles (Figure 2c) while

PEGylated silica NCs remained the original size presumably because PEGylation on surface imparted steric stability to silica NCs in salt solutions. In addition to PEGylation, a variety of other surface properties—positively or negatively charged moieties, for example—can be realized using any of the large number of commercial silane coupling agents, thus demonstrating another advantage of our drug-conjugated silica NCs.[44]

Cellular Internalization. We first compared the silica NCs of 50 and 200 nm, which were fluorescently labeled with rhodamine B isothiocyanate (RITC), in cellular internalization and trafficking studies. The confocal laser scanning microscopy images obtained (Figure 3a) clearly showed a stronger fluorescent signal in HeLa cells incubated with 50 nm NCs as compared to 200 nm NCs, suggesting that the smaller NCs were internalized more efficiently than their larger counterparts. The relative levels of internalization were further quantified using a microplate reader to measure the percentage of the total fluorescent signal internalized by cells normalized to the amount of total cell protein. As expected, 50 nm NCs showed a 3-fold increased cellular internalization efficiency as compared to 200 nm NCs (9.60 and 3.23%/mg for NCs of 50 and 200 nm respectively, Figure 3b).

According to Figure 3a, 50 nm NCs administered to HeLa cells accumulated in the perinuclear region while the majority of 200 nm NCs resided on or near the cell surface. This observation suggests that, in addition to the amount of uptake, NC size might also influence the uptake pathway. In order to probe the mechanism of cellular internalization, we investigated uptake of NCs in HeLa cells in the presence of various biochemical inhibitors of known internalization pathways (Figure 3c). Toxicity due to the inhibitors was negligible (measured by MTT assay). When HeLa cells were
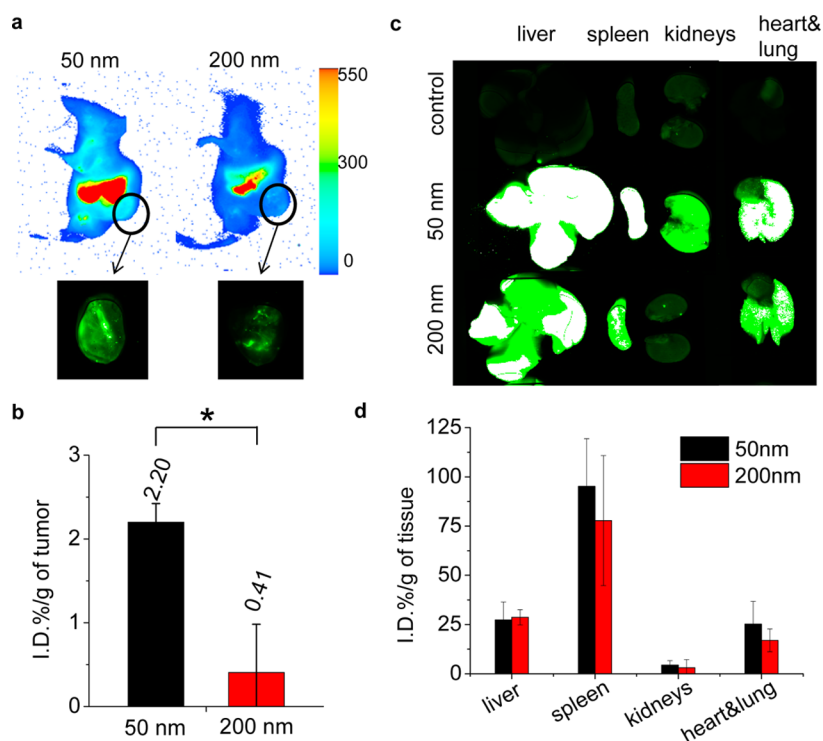
Figure 4. Biodistribution. (a) BALB/c nude mice bearing LNCaP tumors were injected intravenously with 50 and 200 nm silica NCs labeled with IR783. Whole body images were taken by Odyssey infrared mouse imaging system at 800 nm channel. Black circles indicate the positions of tumors. (b−d) Mice were euthanized 24 h post injection. Tumors (b) and other organs (c, d) were collected and measured for total fluorescence intensity (λ_{em} = 800 nm) *ex vivo*. The results were presented as the percentage of total injection dose normalized by gram of the tissue (ID %/g of tumor, average ± SD; n = 3; *p < 0.05).

preincubated with NaN$_3$/2-deoxyglucose (NaN$_3$/DOG)—an inhibitor of cellular adenosine-5′-triphosphate (ATP) synthesis and thus active/energy-dependent endocytosis—for 30 min before adding silica NCs, the cellular internalization for both 50 and 200 nm NCs was significantly decreased (73.5% and 67.6%, respectively) compared to untreated cells. As the internalization of both NCs was not completely inhibited, it is likely that a small portion of the NCs can be internalized through non-energy dependent processes or that exogenous ATP existed in the cell medium.[2] When the cells were pretreated with chlorpromazine, an inhibitor of clathrin-mediated endocytosis, or wortmannin, an inhibitor of macropinocytosis, a significant decrease in internalization was observed for 200 nm NCs (40.2% and 57.0%, respectively) but not for 50 nm NCs. However, when the cells were pretreated with genistein or methyl-β-cyclodextrin (m-βCD)—both are inhibitors of caveolae-mediated uptake—only the internalization of 50 nm NCs was significantly decreased (62.2% and 70.0%, respectively). These results indicated that caveolae-mediated endocytosis played an important role in the internalization of the smaller 50 nm NCs while clathrin and macropinocytosis were the major pathways for 200 nm NCs. Existing literature indicates that caveolar invaginations have diameters of approximately 50−80 nm and can accommodate cell entry of NPs up to 100 nm.[39,44−47] Thus, it is not entirely surprising that 50 nm NCs but not 200 nm NCs enter cells through caveolae-mediated pathways. The diameter of clathrin-coated pits, on the other hand, can be as large as 300 nm,[48,49] and macropinocytosis can be exploited for internalization of even larger NPs (up to 1 μm),[50] thus explaining why these two pathways were more important for 200 nm NC uptake.

Cytotoxicity of Drug−NCs. The cytotoxicity of 50 and 200 nm Cpt−NCs was evaluated and compared with that of free Cpt using a MTT assay. The resultant IC$_{50}$ values for Cpt50 and Cpt200 in LNCaP cells were 510 and 800 nM, respectively (Table 1). The cytotoxicity of the two Cpt−NCs corresponded to the cellular internalization as well as the amount of Cpt released by the two NCs: the 50 nm NCs showed higher toxicity to cancer cells and a lower IC$_{50}$ value as compared to the 200 nm NCs presumably because the smaller NCs experienced more rapid cellular internalization. It is also notable that the *in vitro* MTT assay showed almost no toxicity associated with blank silica NPs (IC$_{50}$ > 1 mM). Recent studies indicated that silica NPs could decompose in the blood within a few days,[51] suggesting that the silica based NPs potentially can be cleared via the renal system.[52,53] Collectively, these observations suggest that the silica-based NC system described here has a suitable biocompatibility and safety profile for potential clinic use.

Biodistribution. As the Cpt−NCs of 50 and 200 nm showed distinct behaviors *in vitro*, we next studied their *in vivo* biodistribution. Biodistribution is one of the key factors that affect the overall therapeutic performance of drug delivery vehicles. As such, silica NCs of 50 and 200 nm were labeled with IR783, a near-infrared dye, and injected into tumor-bearing mice.[39] The near-infrared dye was used to label silica NCs so as to minimize the interference of tissue autofluorescence and fluorescence absorption. The silica NCs were iv administered to BALB/c nude mice bearing LNCaP tumors, and whole body image scans were performed on an Odyssey infrared imaging system 24 h postinjection at λ_{em} = 800 nm with fixed exposure time (Figure 4a, tumors indicated by black circles). Enhanced fluorescence was observed in the tumor of
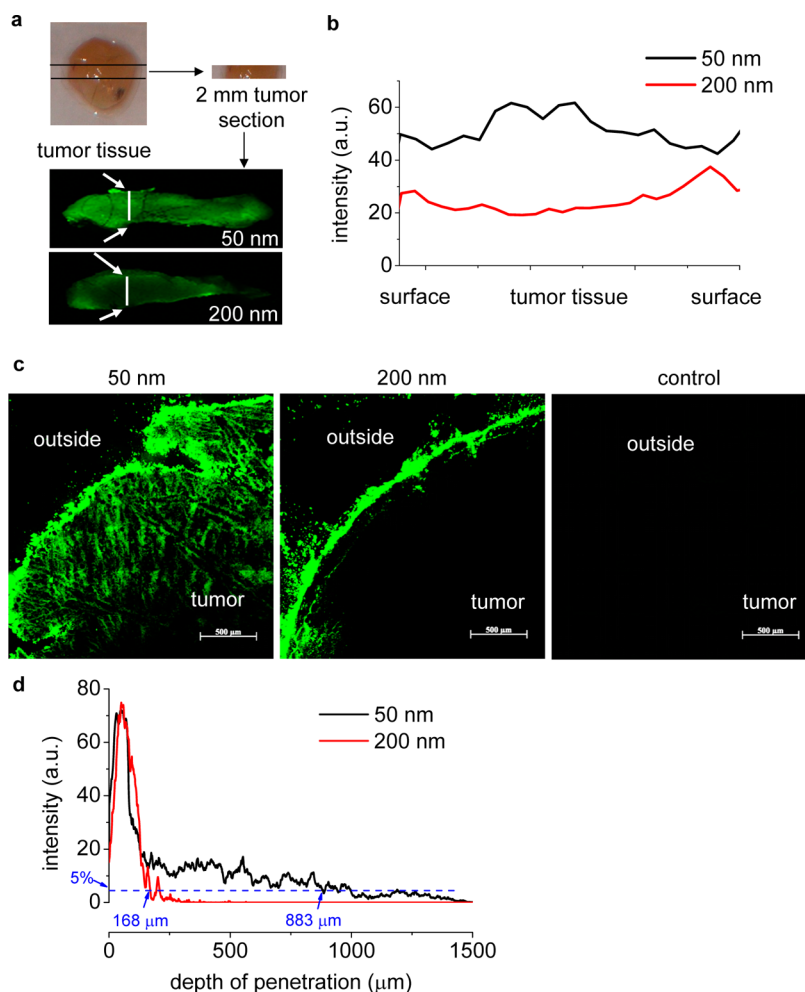
Figure 5. Tumor penetration. (a) Sections of EL4 tumors (~2 mm thickness) collected from C57BL/6 mice which were iv administered with 50 and 200 nm silica NCs labeled with IR783 were collected and placed on glass slides. Fluorescent images were taken by Odyssey infrared imaging system at 800 nm emission. (b) Profile of fluorescent intensity of selected areas (indicated by the lines illustrated in panel a; arrows indicate the surface of tumor sections imaged). (c) EL4 tumors were cultured with 50 or 200 nm silica NCs labeled with IR783 in cell medium for 48 h. Tumors without any treatment served as control. Tumor sections (20 μm in thickness) were collected by cryostat and mounted on glass slides. Fluorescence images were taken by fluorescence microscope with 780 nm laser excitation. An image by tiling 6 × 6 mosaic pictures was taken with fixed exposure time to show the part of edge and center of tumor sections. Scale bar: 500 μm. (d) Fluorescence profile from tumor surface to the inside as shown in panel c was analyzed by Image J.

the mice that received 50 nm NCs while negligible fluorescence was observed in the tumor of the mice dosed with 200 nm NCs. Quantitative measurements of fluorescence intensity in the tumor and other organs were performed *ex vivo* (Figure 4b–d). In an examination of the percentage of the initial dose present in the excised tumor normalized against tumor mass (ID %/g), the tumor accumulation of the 50 and 200 nm NCs 24 h postadministration were 2.2 ± 0.2 and 0.4 ± 0.5 ID %/g (average ± SD; *n* = 3), respectively (Figure 4b). The ~5.5-fold increase in accumulation of 50 nm NCs versus their 200 nm counterparts was statistically significant (*p < 0.05). On the other hand, the accumulation of the two NCs in liver, spleen, kidneys, heart, and lung was not statistically different (Figure 4c,d). As the silica NCs were not functionalized with an active targeting agent, it is likely that the enhanced permeation and retention (EPR) effect plays a major role.[54] The observation that 50 nm NCs were found at significantly higher concentration in the tumor after 24 h indicated that they utilized the EPR effect not only to penetrate into tumor tissue but also to remain within the tumor. Practically, the enhanced

accumulation of 50 nm NCs in tumor suggests that Cpt50 will be able to deliver increased amounts of drug to the disease area and achieve higher efficacy than Cpt200.

Tumor Penetration. To further study the impact of Cpt–NC size on their microdistribution in tumors, we designed both *in vivo* and *ex vivo* tumor penetration studies to compare NCs of 50 and 200 nm. After tumor-bearing mice were administered with IR783-labeled silica NCs of 50 and 200 nm, the tumors were harvested 24 h postinjection and sectioned (~2 mm in thickness). As with the biodistribution study above, mice receiving 50 nm NCs showed greater fluorescence in the tumor tissues compared to mice receiving 200 nm NCs. The 50 nm NCs also were homogeneously distributed throughout the tumor tissue whereas the 200 nm NCs were localized on the tumor surface (Figure 5a). A plot profile of fluorescence intensity versus distance from tumor edge to center was generated by Image J (Figure 5b). Indeed, as predicted in our initial study, higher fluorescence intensity was observed in the tumors treated by 50 nm NCs as opposed to 200 nm NCs. Tumor sections from mice treated with 50 nm NCs also
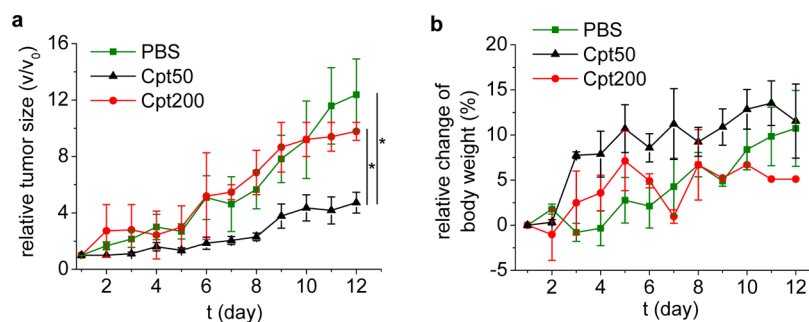
Figure 6. *In vivo* tumor reduction study. (a) Delay and inhibition of LLC tumor growth in C57BL/6 mice with treatment of Cpt−NCs with different sizes. Data are represented as average ± standard error of the mean and analyzed by two-tailed Student's *t* test (*$p < 0.05$). (b) Body weight monitoring over the study.

exhibited an almost homogeneous fluorescence distribution from edge to center while clearly reduced fluorescence intensity was observed in the center of the tumor section treated with 200 nm NCs. This result indicated that, after accumulation in tumor tissues, 50 nm NCs could more thoroughly penetrate the interstitium of tumor tissue thereby potentially reaching tumor cells distant from blood vessels and releasing anticancer drugs to kill the cancer from the inside out.

To more quantitatively evaluate the passive diffusion of silica NCs into tumor tissues, we performed an *ex vivo* tumor penetration study by culturing EL4 tumors harvested from tumor-bearing mice and exposing them to NCs of 50 and 200 nm (IR783-labeled) for 48 h. After incubation, tumor sections of 20 μm thickness were analyzed by fluorescence microscopy at λ_{ex} = 780 nm with fixed exposure time (Figure 5c). Generally, the 50 nm NCs penetrated deeper into the solid tumor with overall higher internal fluorescence intensity than 200 nm NCs. The 200 nm NCs, by comparison, were almost completely localized to the surface of tumors. To quantitatively compare the penetration depth of these different size NCs, the plot profile of fluorescence intensity versus distance from tumor edge to center was generated by Image J (Figure 5d). Penetration depth was defined as the depth at which fluorescence intensity drops to <5% of the maximum intensity at the tumor edge. According to this definition, 50 nm NCs were able to penetrate tumor tissue as deep as 883 μm whereas 200 nm NCs reached a penetration depth of only 168 μm in the EL4 tumors. Collectively, both *ex vivo* (Figure 5a,b) and *in vivo* (Figure 5c,d) studies revealed that 50 nm NCs penetrated tumor tissue more efficiently, likely because the smaller 50 nm NCs had better vascular permeation capability and could diffuse more efficiently into tumor interstitial space.

The distribution of many anticancer drugs and nanomedicines in tumor tissues is incomplete due to the large distance between blood vessels in solid tumors, the composition of the extracellular matrix, cell−cell adhesion, high interstitial fluid pressure, and lack of convection.[55] As such, poor tumor penetration of anticancer drugs is a limiting factor in chemotherapy efficacy.[56] Very recently, substantial effort has been dedicated to improve the tumor penetration of drug.[32,57] Studies have indicated that penetration of NPs into the core of spheroids used as an *in vitro* tumor model is limited to particles smaller than 100 nm.[58] Furthermore, Chan and colleagues reported that 20 and 60 nm gold NPs permeated tumor tissues much more rapidly than 100 nm particles *in vivo*.[1] Based on these results, it is reasonable to expect that Cpt50 with small and monodisperse size may show enhanced solid

tumor penetration than larger drug delivery vehicles, thereby potentially improve their therapeutic efficacy.

***In Vivo* Tumor Reduction Study.** Given the preferential cellular internalization, tumor accumulation, and penetration of 50 nm NCs over 200 nm NCs, we expected the smaller NCs to show improved antitumor efficacy *in vivo*. To explore this, we evaluated the antitumor efficacy of Cpt50 and Cpt200 against LLC tumors induced by subcutaneous injection of LLC cells into the flank of C57BL/6 mice. After tumors reached ∼300 mm³ in size, the animals were divided into three groups (*n* = 5) to minimize body weight and tumor size differences among the groups, and Cpt50 and Cpt200 were administered at a dose of 25 mg Cpt equiv./kg. The tumor size and body weight were subsequently monitored for 12 days postinjection. As expected, the animals that received a single iv injection of Cpt50 showed a statistically significant (*$p < 0.05$, two-tailed *t* test) delay in tumor growth relative to the PBS group (Figure 6a). Statistical significance was also observed between the Cpt50 and Cpt200 groups from day 7 to day 12. Collectively, the observations indicated that Cpt50 had significantly higher efficacy than Cpt200 in inhibiting subcutaneous LLC tumors in mice. No acute body weight drop was observed for all the groups, suggesting no acute toxicity for Cpt−NCs of both sizes (Figure 6b).

The *in vitro* and *in vivo* results presented here clearly demonstrated that size of nanomedicine could greatly impact the overall antitumor efficacy. Specifically, Cpt50 showed greater antitumor efficacy as compared to Cpt200. The enhanced efficacy of smaller drug−NCs is likely due to the improved tumor accumulation and penetration *in vivo,* as well as more efficient cellular internalization and higher cytotoxicity of small NCs compared to their larger counterparts. Although the cytotoxicity of Cpt50 and Cpt200 was not dramatically different *in vitro*—IC$_{50}$'s of 510 nM and 800 nM, respectively— the difference in *in vivo* antitumor efficacy was obvious, suggesting that the enhanced tumor accumulation and penetration are likely the source of the improved performance. As demonstrated in the *ex vivo* tumor study, the 50 nm NCs had substantially faster passive diffusion in tumor tissues. However, the more efficient cellular internalization of 50 nm NCs is also important for the NCs to achieve prolonged retention in tumors, ultimately leading to higher levels of drug released within tumor tissue and cancer cells. We previously showed that both 50 nm and 20 nm NCs were superior to 200 nm NCs in tumor tissue penetration in a subcutaneous murine LLC model.[39] However, because of the ultrasmall size and highly effective passive diffusion inside tissue interstitium, 20 nm NCs may transport rapidly from interstitial spaces in tumor

to lymphatic vessels or the adjacent organs. This results in less sustained tumor accumulation as compared to particles >30 nm and potentially overall reduced efficacy.[1,59,60] Thus, the 50 nm Cpt–NC is likely in the optimized size range (30–50 nm) for the most effective treatment of subcutaneous LLC tumors in mice.

CONCLUSIONS

In this study, we formulated Cpt–NCs with excellent size control and studied the impact of size of nanomedicine on antitumor efficacy. NCs with 50 nm diameter were demonstrated to not only outperform 200 nm NCs in terms of cellular internalization, *in vivo* tumor targeting, and penetration but also improve overall antitumor efficacy. The smaller NCs (50 nm) are likely to outperform larger NCs (200 nm) especially in the treatment of chemotherapy-resistant tumors that will require a higher threshold intracellular concentration for a biologically meaningful objective response. These results strongly emphasize the importance of controlling the size of nanomedicine ≤50 nm to achieve enhanced efficacy. Using the novel drug–silica chemistry described in this article, we can easily prepare monodisperse Cpt–NCs ≤50 nm with excellently controlled size. This formulation strategy holds great potential for further improvement in cancer treatment via size-controlled nanomedicine. We foresee such drug–silica NCs as a clinically relevant drug delivery system which not only offers a unique platform for the further study of the size effect of nanomedicine on the treatment of different cancers but also can be readily prepared with the optimized size on a larger scale for potential clinic applications.

ASSOCIATED CONTENT

Ⓢ Supporting Information

Raw data of DLS measurement. This material is available free of charge via the Internet at http://pubs.acs.org.

AUTHOR INFORMATION

Corresponding Author

*E-mail: jianjunc@illinois.edu.

Notes

The authors declare no competing financial interest.

ACKNOWLEDGMENTS

REFERENCES

(1) Perrault, S. D.; Walkey, C.; Jennings, T.; Fischer, H. C.; Chan, W. C. W. Mediating Tumor Targeting Efficiency of Nanoparticles Through Design. *Nano Lett.* **2009**, *9*, 1909–1915.

(2) Gratton, S. E. A.; Ropp, P. A.; Pohlhaus, P. D.; Luft, J. C.; Madden, V. J.; Napier, M. E.; DeSimone, J. M. The effect of particle design on cellular internalization pathways. *Proc. Natl. Acad. Sci. U.S.A.* **2008**, *105*, 11613–11618.

(3) Jiang, W.; Kim, B. Y. S.; Rutka, J. T.; Chan, W. C. W. Nanoparticle-mediated cellular response is size-dependent. *Nat. Nanotechnol.* **2008**, *3*, 145–150.

(4) Fox, M. E.; Szoka, F. C.; Frechet, J. M. J. Soluble Polymer Carriers for the Treatment of Cancer: The Importance of Molecular Architecture. *Acc. Chem. Res.* **2009**, *42*, 1141–1151.

(5) Alexis, F.; Pridgen, E.; Molnar, L. K.; Farokhzad, O. C. Factors Affecting the Clearance and Biodistribution of Polymeric Nanoparticles. *Mol. Pharmaceutics* **2008**, *5*, 505–515.

(6) Davis, M. E.; Chen, Z.; Shin, D. M. Nanoparticle therapeutics: an emerging treatment modality for cancer. *Nat. Rev. Drug Discovery* **2008**, *7*, 771–782.

(7) Medina, S. H.; Tekumalla, V.; Chevliakov, M. V.; Shewach, D. S.; Ensminger, W. D.; El-Sayed, M. E. H. N-acetylgalactosamine-functionalized dendrimers as hepatic cancer cell-targeted carriers. *Biomaterials* **2011**, *32*, 4118–4129.

(8) Shim, M. S.; Kwon, Y. J. Acid-transforming polypeptide micelles for targeted nonviral gene delivery. *Biomaterials* **2010**, *31*, 3404–3413.

(9) Bae, J. W.; Pearson, R. M.; Patra, N.; Sunoqrot, S.; Vukovic, L.; Kral, P.; Hong, S. Dendron-mediated self-assembly of highly PEGylated block copolymers: a modular nanocarrier platform. *Chem. Commun.* **2011**, *47*, 10302–10304.

(10) Park, J. H.; Gu, L.; von Maltzahn, G.; Ruoslahti, E.; Bhatia, S. N.; Sailor, M. J. Biodegradable luminescent porous silicon nanoparticles for in vivo applications. *Nat. Mater.* **2009**, *8*, 331–336.

(11) Li, L. L.; Tang, F. Q.; Liu, H. Y.; Liu, T. L.; Hao, N. J.; Chen, D.; Teng, X.; He, J. Q. In Vivo Delivery of Silica Nanorattle Encapsulated Docetaxel for Liver Cancer Therapy with Low Toxicity and High Efficacy. *ACS Nano* **2010**, *4*, 6874–6882.

(12) Della Rocca, J.; Huxford, R. C.; Comstock-Duggan, E.; Lin, W. Polysilsesquioxane Nanoparticles for Targeted Platin-Based Cancer Chemotherapy by Triggered Release. *Angew. Chem., Int. Ed.* **2011**, *50*, 10330–10334.

(13) Benezra, M.; Penate-Medina, O.; Zanzonico, P. B.; Schaer, D.; Ow, H.; Burns, A.; DeStanchina, E.; Longo, V.; Herz, E.; Iyer, S.; Wolchok, J.; Larson, S. M.; Wiesner, U.; Bradbury, M. S. Multimodal silica nanoparticles are effective cancer-targeted probes in a model of human melanoma. *J. Clin. Invest.* **2011**, *121*, 2768–2780.

(14) Yan, E. Y.; Fu, Y. L.; Wang, X.; Ding, Y.; Qian, H. Q.; Wang, C. H.; Hu, Y.; Jiang, X. Q. Hollow chitosan-silica nanospheres for doxorubicin delivery to cancer cells with enhanced antitumor effect in vivo. *J. Mater. Chem.* **2011**, *21*, 3147–3155.

(15) Jin, Y. H.; Lohstreter, S.; Pierce, D. T.; Parisien, J.; Wu, M.; Hall, C.; Zhao, J. X. J. Silica nanoparticles with continuously tunable sizes: Synthesis and size effects on cellular contrast Imaging. *Chem. Mater.* **2008**, *20*, 4411–4419.

(16) Meng, H.; Yang, S.; Li, Z. X.; Xia, T.; Chen, J.; Ji, Z. X.; Zhang, H. Y.; Wang, X.; Lin, S. J.; Huang, C.; Zhou, Z. H.; Zink, J. I.; Nel, A. E. Aspect Ratio Determines the Quantity of Mesoporous Silica Nanoparticle Uptake by a Small GTPase-Dependent Macropinocytosis Mechanism. *ACS Nano* **2011**, *5*, 4434–4447.

(17) Lai, C. Y.; Trewyn, B. G.; Jeftinija, D. M.; Jeftinija, K.; Xu, S.; Jeftinija, S.; Lin, V. S. Y. A mesoporous silica nanosphere-based carrier system with chemically removable CdS nanoparticle caps for stimuli-responsive controlled release of neurotransmitters and drug molecules. *J. Am. Chem. Soc.* **2003**, *125*, 4451–4459.

(18) Hulchanskyy, T. Y.; Roy, I.; Goswami, L. N.; Chen, Y.; Bergey, E. J.; Pandey, R. K.; Oseroff, A. R.; Prasad, P. N. Organically modified silica nanoparticles with covalently incorporated photosensitizer for photodynamic therapy of cancer. *Nano Lett.* **2007**, *7*, 2835–2842.

(19) Lu, J.; Liong, M.; Li, Z. X.; Zink, J. I.; Tamanoi, F. Biocompatibility, Biodistribution, and Drug-Delivery Efficiency of Mesoporous Silica Nanoparticles for Cancer Therapy in Animals. *Small* **2010**, *6*, 1794–1805.

(20) Hu, C. M. J.; Zhang, L.; Aryal, S.; Cheung, C.; Fang, R. H.; Zhang, L. F. Erythrocyte membrane-camouflaged polymeric nanoparticles as a biomimetic delivery platform. *Proc. Natl. Acad. Sci. U.S.A.* **2011**, *108*, 10980–10985.

(21) Azzi, J.; Tang, L.; Moore, R.; Tong, R.; El Haddad, N.; Akiyoshi, T.; Mfarrej, B.; Yang, S. M.; Jurewicz, M.; Ichimura, T.; Lindeman, N.; Cheng, J. J.; Abdi, R. Polylactide-cyclosporin A nanoparticles for targeted immunosuppression. *FASEB J.* **2010**, *24*, 3927–3938.

(22) Shangguan, D.; Li, Y.; Tang, Z. W.; Cao, Z. H. C.; Chen, H. W.; Mallikaratchy, P.; Sefah, K.; Yang, C. Y. J.; Tan, W. H. Aptamers evolved from live cells as effective molecular probes for cancer study. *Proc. Natl. Acad. Sci. U.S.A.* **2006**, *103*, 11838−11843.

(23) Tasciotti, E.; Liu, X. W.; Bhavane, R.; Plant, K.; Leonard, A. D.; Price, B. K.; Cheng, M. M. C.; Decuzzi, P.; Tour, J. M.; Robertson, F.; Ferrari, M. Mesoporous silicon particles as a multistage delivery system for imaging and therapeutic applications. *Nat. Nanotechnol.* **2008**, *3*, 151−157.

(24) Tang, L.; Azzi, J.; Kwon, M.; Mounayar, M.; Tong, R.; Yin, Q.; Moore, R.; Skartsis, N.; Fan, T. M.; Abdi, R.; Cheng, J. Immunosuppressive Activity of Size-Controlled PEG-PLGA Nano-particles Containing Encapsulated Cyclosporine A. *J. Transplant.* **2012**, *2012*, No. 896141.

(25) Wagner, V.; Dullaart, A.; Bock, A. K.; Zweck, A. The emerging nanomedicine landscape. *Nat. Biotechnol.* **2006**, *24*, 1211−1217.

(26) Nel, A. E.; Madler, L.; Velegol, D.; Xia, T.; Hoek, E. M. V.; Somasundaran, P.; Klaessig, F.; Castranova, V.; Thompson, M. Understanding biophysicochemical interactions at the nano-bio interface. *Nat. Mater.* **2009**, *8*, 543−557.

(27) Tong, R.; Cheng, J. J. Ring-Opening Polymerization-Mediated Controlled Formulation of Polylactide-Drug Nanoparticles. *J. Am. Chem. Soc.* **2009**, *131*, 4744−4754.

(28) Tong, R.; Cheng, J. J. Paclitaxel-initiated, controlled polymer-ization of lactide for the formulation of polymeric nanoparticulate delivery vehicles. *Angew. Chem., Int. Ed.* **2008**, *47*, 4830−4834.

(29) Sun, X. K.; Rossin, R.; Turner, J. L.; Becker, M. L.; Joralemon, M. J.; Welch, M. J.; Wooley, K. L. An assessment of the effects of shell cross-linked nanoparticle size, core composition, and surface PEGylation on in vivo biodistribution. *Biomacromolecules* **2005**, *6*, 2541−2554.

(30) Tang, L.; Yang, X.; Dobrucki, L. W.; Chaudhury, I.; Yin, Q.; Yao, C.; Lezmi, S.; Helferich, W. G.; Fan, T. M.; Cheng, J. Aptamer-Functionalized, Ultra-Small, Monodisperse Silica Nanoconjugates for Targeted Dual-Modal Imaging of Lymph Nodes with Metastatic Tumors. *Angew. Chem., Int. Ed.* **2012**, *51*, 12721−12726.

(31) Geng, Y.; Dalhaimer, P.; Cai, S. S.; Tsai, R.; Tewari, M.; Minko, T.; Discher, D. E. Shape effects of filaments versus spherical particles in flow and drug delivery. *Nat. Nanotechnol.* **2007**, *2*, 249−255.

(32) Kim, B.; Han, G.; Toley, B. J.; Kim, C.-k.; Rotello, V. M.; Forbes, N. S. Tuning payload delivery in tumour cylindroids using gold nanoparticles. *Nat. Nanotechnol.* **2010**, *5*, 465−472.

(33) Cabral, H.; Matsumoto, Y.; Mizuno, K.; Chen, Q.; Murakami, M.; Kimura, M.; Terada, Y.; Kano, M. R.; Miyazono, K.; Uesaka, M.; Nishiyama, N.; Kataoka, K. Accumulation of sub-100 nm polymeric micelles in poorly permeable tumours depends on size. *Nat. Nanotechnol.* **2011**, *6*, 815−823.

(34) Northfelt, D. W.; Dezube, B. J.; Thommes, J. A.; Miller, B. J.; Fischl, M. A.; Friedman-Kien, A.; Kaplan, L. D.; Du Mond, C.; Mamelok, R. D.; Henry, D. H. Pegylated-liposomal doxorubicin versus doxorubicin, bleomycin, and vincristine in the treatment of AIDS-related Kaposi's sarcoma: results of a randomized phase III clinical trial. *J. Clin. Oncol.* **1998**, *16*, 2445−2451.

(35) Gradishar, W. J.; Tjulandin, S.; Davidson, N.; Shaw, H.; Desai, N.; Bhar, P.; Hawkins, M.; O'Shaughnessy, J. Phase III Trial of Nanoparticle Albumin-Bound Paclitaxel Compared With Polyethy-lated Castor Oil−Based Paclitaxel in Women With Breast Cancer. *J. Clin. Oncol.* **2005**, *23*, 7794−7803.

(36) Unezaki, S.; Maruyama, K.; Hosoda, J.-I.; Nagae, I.; Koyanagi, Y.; Nakata, M.; Ishida, O.; Iwatsuru, M.; Tsuchiya, S. Direct measurement of the extravasation of polyethyleneglycol-coated liposomes into solid tumor tissue by in vivo fluorescence microscopy. *Int. J. Pharm.* **1996**, *144*, 11−17.

(37) Uster, P. S.; Working, P. K.; Vaage, J. Pegylated liposomal doxorubicin (DOXIL®, CAELYX®) distribution in tumour models observed with confocal laser scanning microscopy. *Int. J. Pharm.* **1998**, *162*, 77−86.

(38) Chen, K. J.; Tang, L.; Garcia, M. A.; Wang, H.; Lu, H.; Lin, W. Y.; Hou, S.; Yin, Q.; Shen, C. K. F.; Cheng, J. J.; Tseng, H. R. The

therapeutic efficacy of camptothecin-encapsulated supramolecular nanoparticles. *Biomaterials* **2012**, *33*, 1162−1169.

(39) Tang, L.; Fan, T. M.; Borst, L. B.; Cheng, J. Synthesis and Biological Response of Size-Specific, Monodisperse Drug−Silica Nanoconjugates. *ACS Nano* **2012**, *6*, 3954−3966.

(40) Kim, J. W.; Kim, L. U.; Kim, C. K. Size control of silica nanoparticles and their surface treatment for fabrication of dental nanocomposites. *Biomacromolecules* **2007**, *8*, 215−222.

(41) Ha, S. W.; Camalier, C. E.; Beck, G. R.; Lee, J. K. New method to prepare very stable and biocompatible fluorescent silica nano-particles. *Chem. Commun.* **2009**, 2881−2883.

(42) Martin-Kleiner, I.; Svoboda-Beusan, I.; Gabrilovac, J. PMA and doxorubicin decrease viability, MTT activity and expression of CD10 marker on NALM-1 leukemic cells. *Immunopharmacol. Immunotoxicol.* **2006**, *28*, 411−420.

(43) Sun, S. H.; Zeng, H.; Robinson, D. B.; Raoux, S.; Rice, P. M.; Wang, S. X.; Li, G. X. Monodisperse MFe_2O_4 (M = Fe, Co, Mn) nanoparticles. *J. Am. Chem. Soc.* **2004**, *126*, 273−279.

(44) Caliceti, P.; Veronese, F. M. Pharmacokinetic and biodis-tribution properties of poly(ethylene glycol)-protein conjugates. *Adv. Drug Delivery Rev.* **2003**, *55*, 1261−1277.

(45) Rothberg, K. G.; Heuser, J. E.; Donzell, W. C.; Ying, Y.-S.; Glenney, J. R.; Anderson, R. G. W. Caveolin, a protein component of caveolae membrane coats. *Cell* **1992**, *68*, 673−682.

(46) Anderson, R. G. W. The caveolae membrane system. *Annu. Rev. Biochem.* **1998**, *67*, 199−225.

(47) Kurzchalia, T. V. Partan, R. G. Membrane microdomains and caveolae. *Curr. Opin. Cell Biol.* **1999**, *11*, 424−431.

(48) Wasylewski, Z.; Stryjewski, W.; Waśniowska, A.; Potempa, J.; Baran, K. Effect of calcium binding on conformational changes of staphylococcal metalloproteinase measured by means of intrinsic protein fluorescence. *Biochim. Biophys. Acta* **1986**, *871*, 177−181.

(49) Canton, I.; Battaglia, G. Endocytosis at the nanoscale. *Chem. Soc. Rev.* **2012**, *41*, 2718−2739.

(50) Swanson, J. A. Shaping cups into phagosomes and macro-pinosomes. *Nat. Rev. Mol. Cell Biol.* **2008**, *9*, 639−649.

(51) Finnie, K. S.; Waller, D. J.; Perret, F. L.; Krause-Heuer, A. M.; Lin, H. Q.; Hanna, J. V.; Barbe, C. J. Biodegradability of sol-gel silica microparticles for drug delivery. *J. Sol-Gel Sci. Technol.* **2009**, *49*, 12−18.

(52) Cho, M. J.; Cho, W. S.; Choi, M.; Kim, S. J.; Han, B. S.; Kim, S. H.; Kim, H. O.; Sheen, Y. Y.; Jeong, J. Y. The impact of size on tissue distribution and elimination by single intravenous injection of silica nanoparticles. *Toxicol. Lett.* **2009**, *189*, 177−183.

(53) He, X. X.; Nie, H. L.; Wang, K. M.; Tan, W. H.; Wu, X.; Zhang, P. F. In Vivo Study of Biodistribution and Urinary Excretion of Surface-Modified Silica Nanoparticles. *Anal. Chem.* **2008**, *80*, 9597−9603.

(54) Maeda, H.; Wu, J.; Sawa, T.; Matsumura, Y.; Hori, K. Tumor vascular permeability and the EPR effect in macromolecular therapeutics: a review. *J. Controlled Release* **2000**, *65*, 271−284.

(55) Minchinton, A. I.; Tannock, I. F. Drug penetration in solid tumours. *Nat. Rev. Cancer* **2006**, *6*, 583−592.

(56) Tredan, O.; Galmarini, C. M.; Patel, K.; Tannock, I. F. Drug resistance and the solid tumor microenvironment. *J. Natl. Cancer Inst.* **2007**, *99*, 1441−1454.

(57) Sugahara, K. N.; Teesalu, T.; Karmali, P. P.; Kotamraju, V. R.; Agemy, L.; Greenwald, D. R.; Ruoslahti, E. Coadministration of a Tumor-Penetrating Peptide Enhances the Efficacy of Cancer Drugs. *Science* **2010**, *328*, 1031−1035.

(58) Goodman, T. T.; Olive, P. L.; Pun, S. H. Increased nanoparticle penetration in collagenase-treated multicellullar spheroids. *Int. J. Nanomed.* **2007**, *2*, 265−274.

(59) Moghimi, S. M.; Hunter, A. C.; Murray, J. C. Nanomedicine: current status and future prospects. *FASEB J.* **2005**, *19*, 311−330.

(60) Moghimi, S. M.; Bonnemain, B. Subcutaneous and intravenous delivery of diagnostic agents to the lymphatic system: applications in lymphoscintigraphy and indirect lymphography. *Adv. Drug Delivery Rev.* **1999**, *37*, 295−312.